Available online www.worldscientificnews.com

World Scientific News

An International Scientific Journal

WSN 219 (2026) 123-152 EISSN 2392-2192

Role of Nuclear Scattering Phase Shifts in the Design and Fabrication of Designer Superheavy Nuclei

J. K. Maritim[1], S. K. Rotich[2], and K. M. Khanna[3]

jkmaritim728@gmai.com[1], samkrotich@yahoo.com[2]

Department of Mathematics, Physics and Computing, Moi University[1,2], P.O. Box 3900-30100, Kenya. Department of Physics, University of Eldoret[3], P.O. Box 1125-3010, Kenya.

Correspondence Email: khannak700@gmail.com[3]

https://doi.org/10.65770/BVRM7690

ABSTRACT

Superheavy-element synthesis is controlled by a narrow competition among Coulomb-barrier penetration, capture, quasifission, compound-nucleus formation, and survival against fission. This study develops a phase-shift-guided framework for selecting and evaluating entrance channels for designer superheavy nuclei. The formalism combines a complex Woods–Saxon optical interaction, finite-size Coulomb and spin–orbit terms, partial-wave S-matrix analysis, coupled-channel barrier splitting, Hill–Wheeler transmission and evaporation-residue factorization. CERN Open Data from ALICE and ATLAS Pb–Pb collisions are incorporated as an independent high-energy heavy-ion benchmark for data provenance, event-scale comparison and reproducible analysis practice; they are not used as surrogate near-barrier phase-shift measurements. A transparent $^{48}\mathrm{Ca} + {}^{248}\mathrm{Cm}$ numerical case is used to demonstrate how the interaction potential generates partial-wave phase accumulation, how collective couplings redistribute the fusion barrier, and how the transmitted angular-momentum window changes with energy. The calculations show that phase information is most informative when interpreted jointly with absorption, barrier distributions and compound-nucleus survival. The study further identifies the measurements required to convert the framework into a predictive tool for $Z = 119$–120 searches: near-barrier elastic or quasi-elastic angular distributions, deformation-constrained coupled-channel fits, and uncertainty propagation into capture and evaporation-residue cross sections. The resulting approach provides a reproducible bridge between scattering observables and reaction design while maintaining a strict separation between ultra-relativistic CERN Pb–Pb data and low-energy superheavy-nucleus formation physics.

Keywords: superheavy nuclei, scattering phase shifts, optical model, Woods–Saxon potential, coupled channels, heavy-ion fusion, CERN Open Data, Pb–Pb collisions, island of stability.

(Received 7 July 2026; Accepted 15 August 2026; Date of Publication 25 September 2026)

1. INTRODUCTION AND LITERATURE REVIEW

The extension of the periodic table into the superheavy region is a problem in reaction dynamics as much as in nuclear structure. Shell corrections may stabilize nuclei against prompt fission, yet the entrance channel must first overcome the Coulomb barrier, avoid reseparation through quasifission, equilibrate into a compound nucleus and survive de-excitation by neutron evaporation [1], [2]. The observed evaporation-residue cross section is therefore the product of several small probabilities [3]. Experiments based on $^{48}\mathrm{Ca}$ projectiles and actinide targets established elements through $Z = 118$and demonstrated that increasing neutron number leads toward enhanced stability associated with the predicted $N = 184$ shell region [4].

In this work, the term designer superheavy nucleus denotes a nucleus whose intended proton number, neutron number, excitation energy and angular-momentum population are approached by deliberate optimization of the projectile, target, beam energy and entrance-channel couplings. The term does not imply deterministic fabrication of a prescribed isotope. Rather, it emphasizes rational reaction design under severe probabilistic constraints.

Scattering phase shifts provide a natural language for this optimization. In a partial-wave description, the phase shift and inelasticity determine the S-matrix, while the loss of elastic flux controls the reaction probability [5], [6]. Phase shifts are sensitive to the radial form, surface diffuseness, absorption and deformation couplings of the nucleus–nucleus interaction [7]. They therefore link elastic scattering to barrier penetration, resonance-like structure and reaction-channel competition.

CERN Open Data provide an additional, but distinct, contribution to this program. The ALICE and ATLAS experiments have released Pb–Pb collision samples at TeV energies with event counts ranging from hundreds of thousands to more than 2×10^8events [8], [9]. These data probe quark–gluon plasma and ultra-relativistic nuclear dynamics, not the near-Coulomb-barrier fusion process used to create superheavy elements. Their value here is methodological: they provide real heavy-ion collision records, documented event statistics, reproducible analysis environments and examples of centrality-based event classification. The present paper explicitly preserves this energy-scale separation.

1.1. Superheavy-Element Synthesis and Current Literature

The successful $^{48}\mathrm{Ca}$-induced program at Dubna used targets from $^{238}\mathrm{U}$ through $^{249}\mathrm{Cf}$ and produced isotopes of elements 112–118. Oganessian et al. reviewed production cross sections, decay chains and the progressive stabilization of neutron-richer superheavy nuclei [10]. Contemporary reaction design must move beyond a single optimum beam energy and account for capture, quasifission, shell effects, neutron separation energies and fission barriers. Candidate reactions involving $^{50}\mathrm{Ti}$ and heavier projectiles are of particular interest for $Z \geq 119$ because suitable targets beyond californium are limited [11].

1.2. Phase Shifts as Reaction-Design Observables

For a central interaction, the elastic scattering amplitude is determined by the complete set of partial-wave S-matrix elements [12]. A rapidly changing phase shift signals strong interaction or resonant trapping, whereas the magnitude of the S-matrix measures survival of elastic flux [13].

In an absorptive heavy-ion optical model, the same interaction that modifies the elastic phase also controls the probability that flux enters capture, transfer, deep-inelastic, or fusion-like channels [14]. Phase-shift analysis is therefore most useful when combined with independent reaction observables and coupled-channel calculations rather than interpreted as a stand-alone predictor of evaporation residues.

1.3. Coupled-Channel Dynamics and Research Gap

Collective rotational and vibrational degrees of freedom split a nominal Coulomb barrier into a distribution of eigen-barriers. This effect enhances sub-barrier capture and is routinely described by coupled-channel calculations. Woods–Saxon diffuseness and deformation couplings can strongly affect the predicted excitation function, motivating simultaneous constraints from elastic scattering, inelastic channels, and fusion data [15], [16].

2. THEORETICAL FRAMEWORK

Throughout this section, E denotes the center-of-mass energy, μ the reduced mass, J the conserved total angular momentum in coupled-channel calculations, l the orbital angular momentum in a single-channel reduction, α and β channel quantum numbers, η the Sommerfeld parameter, σ_l the Coulomb phase, δ_l the nuclear phase shift, and S^N the Coulomb-reduced nuclear S-matrix. This notation prevents the Coulomb phase from being conflated with the nuclear interaction phase.

2.1. Relative-Motion Schrödinger Equation

For projectile P and target T, the relative-motion wave function satisfies

$$\left[-\frac{\hbar^2}{2\mu}\nabla^2 + U(r,\{\xi\},E) - E\right]\Psi(r,\{\xi\}) = 0, \qquad (1)$$

where $\{\xi\}$ represents the intrinsic degrees of freedom of the colliding nuclei [17].

The reduced mass is

$$\mu = \frac{m_P m_T}{m_P + m_T}, \qquad (2)$$

and the asymptotic wave number is

$$k = \frac{\sqrt{2\mu E}}{\hbar}. \qquad (3)$$

2.2. Complex Optical Potential

The entrance-channel interaction is represented by

$$U(r,E) = V_N(r,E) + V_C(r) + V_{SO}(r,E) + iW(r,E). \qquad (4)$$

The real nuclear interaction is represented using a Woods–Saxon potential [18],

$$V_N(r) = -\frac{V_0}{1+\exp[(r-R_V)/a_V]}, \qquad (5)$$

$V_N(r)$ is the real nuclear interaction potential between the projectile and target at center-to-center separation r, expressed in MeV.

r is the radial separation between the centers of mass of the projectile and target nuclei, normally expressed in femtometres (fm).

V_0 is the depth of the real Woods–Saxon potential, expressed in MeV. The negative sign in Eq. (5) indicates that the nuclear contribution is attractive, where

$$R_V = r_V\left(A_P^{1/3} + A_T^{1/3}\right). \tag{6}$$

R_V is the effective radius of the real nuclear potential, in fm. It approximately specifies the radial position at which the Woods–Saxon potential falls to one-half of its interior magnitude, since $V_N(R_V) = -V_0/2$.

a_V is the surface diffuseness parameter, in fm. It controls how rapidly the nuclear potential changes from its interior value to approximately zero across the nuclear surface. A larger $a_V$corresponds to a more diffuse interaction surface.

r_V is the reduced nuclear-radius parameter, in fm, used to construct the effective projectile–target interaction radius.

A_P is the mass number of the projectile nucleus; for the representative $^{48}\mathrm{Ca}$ projectile, $A_P = 48$.

A_T is the mass number of the target nucleus; for the representative $^{248}\mathrm{Cm}$ target, $A_T = 248$.

$A_P^{1/3}$ and $A_T^{1/3}$ describe the approximate nuclear-radius scaling with mass number, reflecting the nearly constant bulk density of nuclei.

For the representative reaction

$$^{48}\mathrm{Ca} + {}^{248}\mathrm{Cm}, \tag{6a}$$

Eq. (6) becomes

$$R_V = r_V\left(48^{1/3} + 248^{1/3}\right). \tag{6b}$$

Using the baseline value $r_V = 1.20$ fm,

$$R_V \approx 1.20\left(48^{1/3} + 248^{1/3}\right) \approx 11.9 \text{ fm}. \tag{6c}$$

Thus, Eqs. (5) and (6) collectively specify the strength, radial extent, and surface geometry of the attractive nuclear interaction, which directly influence the calculated scattering phase shifts, effective fusion barrier, transmission coefficients, and ultimately the predicted capture probability for the superheavy-nucleus synthesis reaction.

The imaginary volume term is

$$W_V(r) = -\frac{W_0}{1+\exp[(r-R_W)/a_W]}. \tag{7}$$

A derivative surface contribution may additionally be included when experimental elastic-scattering data require enhanced peripheral absorption.

2.3. Finite-Size Coulomb Interaction

For the effective uniformly charged spherical configuration, the Coulomb potential is written [19]

$$V_C(r) = \begin{cases} \frac{Z_P Z_T e^2}{2R_C}\left(3 - \frac{r^2}{R_C^2}\right), & r < R_C, \\ \frac{Z_P Z_T e^2}{r}, & r \geq R_C. \end{cases} \tag{8}$$

The Coulomb radius is parameterized as

$$R_C = r_C\left(A_P^{1/3} + A_T^{1/3}\right). \tag{9}$$

2.4. Spin–Orbit Interaction

The Thomas-form spin–orbit interaction is represented by [20]

$$V_{\mathrm{SO}}(r) = \lambda_{\mathrm{SO}}\left(\frac{\hbar}{m_\pi c}\right)^2 \frac{1}{r}\frac{df_{\mathrm{SO}}(r)}{dr} L \cdot S, \tag{10}$$

where

$$f_{\mathrm{SO}}(r) = \left[1 + \exp\left(\frac{r - R_{\mathrm{SO}}}{a_{\mathrm{SO}}}\right)\right]^{-1}. \tag{11}$$

The angular operator has eigenvalue

$$L \cdot S = \frac{\hbar^2}{2}[j(j+1) - l(l+1) - s(s+1)]. \tag{12}$$

2.5. Partial-Wave Representation and Complex Phase Shifts

For a central interaction,

$$\Psi(r) = \sum_{l=0}^{\infty} \frac{u_l(r)}{r} P_l(\cos\theta). \tag{13}$$

The radial equation becomes

$$\left[\frac{d^2}{dr^2} + k^2 - \frac{l(l+1)}{r^2} - \frac{2\mu}{\hbar^2}U(r,E)\right]u_l(r) = 0. \tag{14}$$

The Coulomb-reduced nuclear S-matrix is parameterized as [21]

$$S_l^N(E) = \eta_l(E)e^{2i\delta_l(E)},\ 0 \leq \eta_l \leq 1. \tag{15}$$

The complete partial-wave S-matrix contains the Coulomb phase,

$$S_l(E) = e^{2i\sigma_l(E)} S_l^N(E), \tag{16}$$

with

$$\sigma_l = \arg\Gamma\,(l + 1 + i\eta). \tag{17}$$

The Sommerfeld parameter is

$$\eta = \frac{Z_P Z_T e^2 \mu}{\hbar^2 k}. \tag{18}$$

The Coulomb-modified scattering amplitude is therefore

$$f(\theta) = f_C(\theta) + \frac{1}{2ik}\sum_{l=0}^{\infty}(2l+1)e^{2i\sigma_l}[S_l^N(E) - 1]P_l(\cos\theta). \tag{19}$$

The elastic differential cross section follows as

$$\frac{d\sigma_{\text{el}}}{d\Omega} = |f(\theta)|^2. \tag{20}$$

The reaction probability for a given partial wave is

$$P_l^R(E) = 1 - |S_l^N(E)|^2 = 1 - \eta_l^2(E). \tag{21}$$

Accordingly,

$$\sigma_R(E) = \frac{\pi}{k^2}\sum_{l=0}^{\infty}(2l+1)[1 - |S_l^N(E)|^2]. \tag{22}$$

2.6. Phase Accumulation and Wigner Time Delay

For a semiclassical impact parameter

$$b = \frac{l+\frac{1}{2}}{k}, \tag{23}$$

The nuclear eikonal phase, usually denoted by $\chi_N(b)$, is the phase accumulated by the projectile wave function as it passes through the nuclear interaction field of the target along an approximately straight-line trajectory characterized by the impact parameter b. In the eikonal or high-energy semiclassical approximation, it is written as

$$\chi_N(b) = -\frac{1}{\hbar v}\int_{-\infty}^{+\infty} V_N\left(\sqrt{b^2+z^2}\right)dz. \tag{24}$$

where $V_N(r)$ is the nuclear interaction potential, v is the projectile–target relative velocity, $b$is the impact parameter, $z$is the coordinate along the incident trajectory, $r = \sqrt{b^2+z^2}$ is the instantaneous projectile–target separation, and $\hbar$is the reduced Planck constant. Physically, $\chi_N(b)$ measures how strongly the nuclear potential changes the phase of the incident matter wave relative to free propagation. Small b trajectories penetrate more deeply into the nuclear interaction region and generally acquire larger phase modifications, whereas large-b trajectories experience progressively weaker nuclear effects. In the semiclassical correspondence between impact parameter and orbital angular momentum, $b \simeq \frac{l+\frac{1}{2}}{k}$, the eikonal phase can be related approximately to the nuclear partial-wave phase shift by

$$\delta_l^N \simeq \frac{1}{2}\chi_N(b). \tag{25}$$

For your manuscript, it is important to state that the straight-line eikonal approximation is principally a high-energy or weak-deflection approximation. Near the Coulomb barrier in superheavy-element synthesis, strong Coulomb deflection and channel coupling can make the simple eikonal expression quantitatively inadequate; the full Schrödinger/coupled-channel calculation should therefore remain the primary method for obtaining the phase shifts.

The energy derivative of the real phase shift gives the Wigner time delay [22],

$$\tau_l(E) = 2\hbar \frac{d\delta_l^{(R)}}{dE}. \tag{26}$$

For a multichannel problem, the more general Wigner–Smith matrix is

$$Q(E) = -i\hbar S^{\dagger}(E) \frac{dS(E)}{dE}. \tag{27}$$

Its eigenvalues characterize channel-dependent collision delay times [23].

2.7. Barrier Transmission and Capture Cross Section

Near the maximum of the effective interaction barrier, the potential for a given partial wave $l$may be approximated locally by an inverted parabola. The centrifugal term raises the effective barrier above the s-wave value according to [24], [25]

$$V_{B,l} = V_B + \frac{\hbar^2 l(l+1)}{2\mu R_B^2}. \tag{28}$$

Within the Hill–Wheeler approximation, the transmission coefficient is

$$T_l(E) = \left[1 + \exp\left(\frac{2\pi[V_{B,l} - E]}{\hbar\omega_l}\right)\right]^{-1}, \tag{29}$$

where $\hbar\omega_l$ denotes the curvature of the effective barrier.

The total capture cross section is therefore

$$\sigma_{\text{cap}}(E) = \frac{\pi}{k^2} \sum_{l=0}^{\infty} (2l + 1)\, T_l(E). \tag{30}$$

For a coupled-channel system, the single nominal barrier is replaced by a set of effective eigenbarriers. The capture cross section may then be approximated by

$$\sigma_{\text{cap}}^{\text{CC}}(E) = \sum_i w_i \; \sigma_{\text{cap}}(E; V_B + \Delta_i), \tag{31}$$

subject to $\sum_i w_i = 1$. Here $\Delta_i$is the displacement of the i-th eigenbarrier relative to the nominal barrier and $w_i$is its weight.

2.8. Evaporation-Residue Formation

Capture does not guarantee successful superheavy-nucleus formation. After barrier penetration, the dinuclear configuration may undergo quasifission or evolve into a statistically equilibrated compound nucleus [26]. The evaporation-residue cross section is therefore written as

$$\sigma_{\text{ER}}(E) = \sum_{J=0}^{\infty} \sigma_{\text{cap}}(E, J)\, P_{\text{CN}}(E, J)\, W_{\text{sur}}(E^*, J). \tag{32}$$

The partial-wave capture contribution is

$$\sigma_{\text{cap}}(E, J) = \frac{\pi}{k^2}(2J + 1)\, T_J(E). \tag{33}$$

In this expression, P_{CN} is the probability that the captured system reaches a fully equilibrated compound-nucleus configuration, while W_{sur} is the probability that the excited compound nucleus survives fission during de-excitation.

A local sensitivity matrix may be defined by

$$J_{ij} = \frac{\partial O_i}{\partial \theta_j}, \tag{34}$$

where O_i represents a calculated observable and θ_j denotes a model parameter.

The survival probability for an xn-evaporation channel may be expressed as

$$W_{\text{sur}}^{(xn)}(E^*, J) = \prod_{i=1}^{x} \frac{\Gamma_n(E_i^*, J)}{\Gamma_n(E_i^*, J) + \Gamma_f(E_i^*, J) + \sum_c \Gamma_c(E_i^*, J)}. \tag{35}$$

This equation makes clear why maximum capture does not necessarily imply maximum evaporation-residue yield.

2.9. Compound-Nucleus Excitation Energy

The compound-nucleus excitation energy is

$$E^* = E_{\text{c.m.}} + Q, \tag{36}$$

where Q is the reaction Q-value under the adopted sign convention.

An optimum synthesis window generally lies above the capture threshold but sufficiently low that fission competition remains suppressed.

2.10. Fusion-Barrier Distribution

The fusion-barrier distribution may be obtained from

$$D_{\text{fus}}(E) = \frac{d^2}{dE^2}[E\sigma_{\text{fus}}(E)]. \tag{37}$$

Here, $D_{\text{fus}}(E)$ is the fusion-barrier distribution, which characterizes the distribution of effective Coulomb–nuclear barriers generated by couplings between the relative motion and intrinsic nuclear degrees of freedom; E is the projectile–target center-of-mass energy, normally expressed in MeV; and $\sigma_{\text{fus}}(E)$ is the total fusion cross section at energy E, typically expressed in barns (b), millibarns (mb), or femtometres squared (fm^2). The operator d^2/dE^2 denotes the second derivative with respect to center-of-mass energy. Consequently, $E\sigma_{\text{fus}}(E)$ is the energy-weighted fusion cross section, and peaks in $D_{\text{fus}}(E)$ reveal effective barriers arising from nuclear deformation, rotational or vibrational excitation, transfer coupling, and other channel-coupling effects.

For experimental or discretely calculated excitation functions, Eq. (37) may be evaluated numerically as $D_{\text{fus}}(E_i) \approx \frac{(E\sigma)_{i+1} - 2(E\sigma)_i + (E\sigma)_{i-1}}{(\Delta E)^2}$, where ΔE is the energy spacing.

In an eigenchannel approximation,

$$\sigma_{\text{fus}}^{\text{CC}}(E) = \sum_\alpha w_\alpha \, \sigma_{\text{fus}}(E; B_\alpha), \tag{38}$$

where B_α and w_α are the effective barrier energies and their weights.

2.11. Coulomb-Wave Matching

The numerical logarithmic derivative at the matching radius r_m is [27]

$$L_l(r_m) = \frac{u_l'(r_m)}{u_l(r_m)}. \quad (39)$$

Here, $L_l(r_m)$is the logarithmic derivative of the radial scattering wave function for the l-th partial wave evaluated at the matching radius; $u_l(r)$is the reduced radial wave function obtained by solving the radial Schrödinger equation; $u_l'(r_m)$is its first radial derivative, $u_l'(r_m) = \left.\frac{du_l(r)}{dr}\right|_{r=r_m}$;

$l = 0,1,2, \ldots$is the orbital angular-momentum quantum number; and $r_m$is the asymptotic matching radius, chosen sufficiently far outside the short-range nuclear interaction for the numerical solution to be matched reliably to the known Coulomb scattering functions. Since u_l'/u_l has dimensions of inverse length, $[L_l] = \mathrm{fm}^{-1}$.

The logarithmic derivative is particularly useful numerically because the overall normalization of $u_l(r)$ cancels. Thus, Eq. (39) provides the bridge between the numerically propagated interior wave function and the asymptotic Coulomb solution from which the scattering phase shift and S-matrix are determined.

The complete Coulomb-modified scattering amplitude is [28]

$$f(\theta) = f_C(\theta) + \frac{1}{2ik}\sum_{l=0}^{\infty}(2l+1)e^{2i\sigma_l}[S_l^N(E) - 1]P_l(\cos\theta). \quad (40)$$

The pure Coulomb amplitude is [29]

$$f_C(\theta) = -\frac{\eta}{2k\sin^2(\theta/2)}\exp\left[2i\sigma_0 - i\eta\ln\left(\sin^2\frac{\theta}{2}\right)\right]. \quad (41)$$

The elastic differential cross section is

$$\frac{d\sigma_{\mathrm{el}}}{d\Omega} = | f(\theta) |^2. \quad (42)$$

The reaction cross section associated with the l-th partial wave is

$$\sigma_l^R = \frac{\pi}{k^2}(2l+1)[1- | S_l^N |^2]. \quad (43)$$

The phase shift follows from Coulomb matching:

$$\tan\delta_l^N = \frac{kF_l'(\eta,kr_m) - L_lF_l(\eta,kr_m)}{L_lG_l(\eta,kr_m) - kG_l'(\eta,kr_m)}. \quad (44)$$

Here, δ_l^N is the nuclear phase shift for partial wave l after separating the known long-range Coulomb phase; l is the orbital angular-momentum quantum number; and $k$is the asymptotic projectile–target wave number, $k = \frac{\sqrt{2\mu E}}{\hbar}$, where μ is the projectile–target reduced mass, E is the center-of-mass energy, and $\hbar$ is the reduced Planck constant.

The quantity η is the Sommerfeld parameter, $\eta = \frac{Z_P Z_T e^2\mu}{\hbar^2 k} = \frac{Z_P Z_T e^2}{\hbar v}$, where Z_P and Z_T are the projectile and target atomic numbers, $e$is the elementary charge, and $v$is their asymptotic relative velocity.

$F_l(\eta,\rho)$ is the regular Coulomb wave function, whereas $G_l(\eta,\rho)$ is the irregular Coulomb wave function, with the dimensionless radial variable $\rho = kr$. At the matching point, $\rho_m = kr_m$.

The quantities F_l' and G_l' denote derivatives of the Coulomb functions with respect to their dimensionless radial argument ρ: $F_l' = \frac{\partial F_l(\eta,\rho)}{\partial \rho}$, $G_l' = \frac{\partial G_l(\eta,\rho)}{\partial \rho}$.

Accordingly, the factors of k in Eq. (44) convert these derivatives into derivatives with respect to the physical radial coordinate r.

Finally, $L_l \equiv L_l(r_m)$ is the logarithmic derivative defined in Eq. (39). Equation (44) therefore determines the nuclear phase shift by matching the numerical Schrödinger solution to the analytically known Coulomb functions outside the nuclear interaction region.

2.12. Deformed-Nucleus Interaction

For a deformed target nucleus [30],

$$R_T(\theta) = R_0\left[1 + \sum_{\lambda=2,4,\ldots} \beta_\lambda Y_{\lambda 0}(\theta)\right]. \quad (45)$$

The leading coupling interaction is

$$V_{\text{coup}}(r,\theta) \simeq -R_0 \frac{dV_N(r)}{dr} \sum_\lambda \beta_\lambda Y_{\lambda 0}(\theta). \quad (46)$$

2.13. Coupled-Channel Matrix Elements

The coupling matrix is

$$V_{\alpha\beta}(r) = \langle \phi_\alpha | V_N(r,\{\xi\}) + V_C(r,\{\xi\}) | \phi_\beta \rangle. \quad (47)$$

The coupled radial equations are

$$\left[-\frac{\hbar^2}{2\mu}\frac{d^2}{dr^2} + \frac{\hbar^2 l_\alpha(l_\alpha+1)}{2\mu r^2} + \epsilon_\alpha - E\right] u_\alpha(r) + \sum_\beta V_{\alpha\beta}(r) u_\beta(r) = 0. \quad (48)$$

2.14. Complex Phase Shifts and Absorption

The phase shift is generally complex [31],

$$\delta_l = \delta_l^R + i\delta_l^I. \quad (49)$$

The nuclear S-matrix becomes

$$S_l^N(E) = \exp[2i\delta_l^R(E) - 2\delta_l^I(E)]. \quad (50)$$

Its modulus is

$$|S_l^N|^2 = \exp[-4\delta_l^I(E)]. \quad (51)$$

The reaction probability is

$$P_l^R(E) = 1 - |S_l^N(E)|^2, \quad (52)$$

and the total reaction cross section is

$$\sigma_R(E) = \frac{\pi}{k^2} \sum_l (2l+1) P_l^R(E). \quad (53)$$

2.15. Fusion-Barrier Curvature

Near the barrier maximum,

$$V_{\mathrm{eff},l}(r) \simeq V_{B,l} - \frac{1}{2}\mu\omega_l^2\left(r - R_{B,l}\right)^2. \tag{54}$$

The corresponding Hill–Wheeler transmission coefficient is [32]

$$T_l(E) = \left[1 + \exp\left(\frac{2\pi[V_{B,l}-E]}{\hbar\omega_l}\right)\right]^{-1}. \tag{55}$$

The fusion-barrier distribution is again [33]

$$D_{\mathrm{fus}}(E) = \frac{d^2}{dE^2}\left[E\sigma_{\mathrm{fus}}(E)\right]. \tag{56}$$

2.16. Link to Designer Superheavy Nuclei

The complete reaction-design sequence is

$$\text{Entrance interaction} \rightarrow S_l \rightarrow T_l \rightarrow \sigma_{\mathrm{cap}} \rightarrow P_{\mathrm{CN}} \rightarrow W_{\mathrm{sur}} \rightarrow \sigma_{\mathrm{ER}}. \tag{57}$$

Although Eq. (57) is a reaction-chain relation rather than an algebraic equation, each quantity has a precise physical meaning.

The entrance interaction is the complete projectile–target interaction governing the initial collision. In the optical-model description it contains the nuclear, Coulomb, absorptive, centrifugal, spin–orbit, and where applicable coupled-channel contributions.

S_l is the partial-wave scattering-matrix element. For the Coulomb-reduced nuclear interaction, $S_l^N(E) = \eta_l(E)e^{2i\delta_l^N(E)}$, where η_l is the inelasticity and δ_l^N is the nuclear phase shift. T_l is the partial-wave transmission or absorption probability, $T_l(E) = 1-|\, S_l^N(E)\,|^2$.

It measures the fraction of incident flux removed from the elastic channel. In a fusion calculation with appropriate boundary conditions, it represents the probability that the l-th partial wave penetrates the entrance-channel barrier.

σ_{cap} is the capture cross section, $\sigma_{\mathrm{cap}}(E) = \frac{\pi}{k^2}\sum_l (2l+1)T_l(E)$, representing formation of a trapped or touching projectile–target configuration after barrier penetration.

P_{CN} is the compound-nucleus formation probability, $0 \le P_{\mathrm{CN}} \le 1$, which gives the probability that a captured dinuclear system proceeds to a fully equilibrated compound nucleus instead of reseparating through quasifission or related competing processes.

W_{sur} is the survival probability of the excited compound nucleus against fission during its de-excitation cascade. It depends on excitation energy E^*, angular momentum J, neutron-separation energies, fission barriers, level densities, shell corrections, and the competing neutron-emission and fission widths.

Finally, σ_{ER} is the evaporation-residue production cross section, representing the experimentally relevant cross section for producing a surviving superheavy nucleus. The complete relation is

$$\sigma_{\mathrm{ER}}(E) = \sum_l \sigma_{\mathrm{cap},l}(E) P_{\mathrm{CN}}(E,l) W_{\mathrm{sur}}(E^*,l). \quad (58)$$

Thus, Eq. (57) summarizes the central physical logic of the paper: the entrance-channel interaction determines the scattering S-matrix and phase shifts; these determine barrier transmission and capture; capture competes with quasifission to form the compound nucleus; and the compound nucleus must subsequently survive fission to produce an observable superheavy evaporation residue.

3. METHODOLOGY

The CERN Open Data component and the near-barrier nuclear-reaction calculation are treated independently. The CERN records provide ultra-relativistic Pb–Pb heavy-ion benchmarks, whereas the optical-model phase shifts are calculated from low-energy nuclear potentials [34], [35].

A representative ALICE charged-particle multiplicity benchmark is

$$\frac{dN_{\mathrm{ch}}}{d\eta} = 1943 \pm 54. \quad (59)$$

The low-energy radial Schrödinger equation is

$$\frac{d^2u_l}{dr^2} + \left[k^2 - \frac{l(l+1)}{r^2} - \frac{2\mu}{\hbar^2}\left(U_N(r,E) + V_C(r)\right)\right] u_l(r) = 0. \quad (60)$$

The asymptotic wave number is

$$k = \frac{\sqrt{2\mu E}}{\hbar}. \quad (61)$$

The total complex interaction is

$$U(r,E) = V_C(r) + V_N(r,E) + iW_N(r,E) + V_{\mathrm{so}}(r)\, L \cdot S. \quad (62)$$

The radial grid is

$$r_n = r_{\min} + nh,\ n = 0,1,\dots,N. \quad (63)$$

Defining

$$Q_l(r) = k^2 - \frac{l(l+1)}{r^2} - \frac{2\mu}{\hbar^2} U(r), \quad (64)$$

gives

$$u_l''(r) + Q_l(r) u_l(r) = 0. \quad (65)$$

The Numerov update is

$$u_{n+1} = \frac{2\left(1 - \frac{5h^2Q_n}{12}\right)u_n - \left(1 + \frac{h^2Q_{n-1}}{12}\right)u_{n-1}}{1 + \frac{h^2Q_{n+1}}{12}}. \quad (66)$$

The origin behavior is

$$u_l(r) \propto r^{l+1},\ r \to 0. \quad (67)$$

Numerical initialization may be taken as

$$u_l(r_1) = r_1^{l+1},\ u_l(r_2) = r_2^{l+1}. \tag{68}$$

The Coulomb asymptotic form is

$$u_l(r) \to \frac{i}{2}\left[H_l^{(-)}(\eta, kr) - S_l^N H_l^{(+)}(\eta, kr)\right], \tag{69}$$

with

$$H_l^{(\pm)} = G_l \pm iF_l. \tag{70}$$

The Sommerfeld parameter is

$$\eta = \frac{Z_P Z_T e^2 \mu}{\hbar^2 k}. \tag{71}$$

The logarithmic derivative is

$$L_l(r_m) = \frac{u_l'(r_m)}{u_l(r_m)}. \tag{72}$$

The matching equation is

$$L_l = \frac{F_l' \cos\delta_l + G_l' \sin\delta_l}{F_l \cos\delta_l + G_l \sin\delta_l}. \tag{73}$$

Therefore,

$$\tan\delta_l = \frac{L_l F_l - F_l'}{G_l' - L_l G_l}. \tag{74}$$

Hence,

$$\delta_l = \tan^{-1}\left[\frac{L_l F_l - F_l'}{G_l' - L_l G_l}\right]. \tag{75}$$

The complex phase shift is

$$\delta_l = \delta_l^{(R)} + i\delta_l^{(I)}. \tag{76}$$

The nuclear S-matrix is

$$S_l^N(E) = \eta_l(E) e^{2i\delta_l^{(R)}(E)} = \exp\left[2i\delta_l^{(R)} - 2\delta_l^{(I)}\right]. \tag{77}$$

The inelasticity is

$$\eta_l(E) = \mid S_l^N(E) \mid = \exp\left[-2\delta_l^{(I)}(E)\right]. \tag{78}$$

The reaction probability is

$$P_l(E) = 1 - \mid S_l^N(E) \mid^2. \tag{79}$$

The total reaction cross section is

$$\sigma_R(E) = \frac{\pi}{k^2} \sum_{l=0}^{l_{\max}} (2l+1)[1 - \mid S_l^N(E) \mid^2]. \tag{80}$$

The capture cross section is

$$\sigma_{\text{cap}}(E) = \frac{\pi}{k^2} \sum_l (2l+1) T_l(E), \tag{81}$$

with

$$T_l(E) = 1 - | S_l^N(E) |^2. \tag{82}$$

Finally,

$$\sigma_{\text{ER}}(E) = \frac{\pi}{k^2} \sum_l (2l+1) T_l(E) P_{\text{CN}}(E,l) W_{\text{sur}}(E^*,l). \tag{83}$$

For an isolated resonance,

$$\delta_l^R(E_R) \simeq \left(n + \frac{1}{2}\right)\pi. \tag{84}$$

The corresponding approximate resonance width is

$$\Gamma \simeq \frac{2}{\left.\frac{d\delta_l^R}{dE}\right|_{E_R}}. \tag{85}$$

The Wigner–Smith time-delay matrix is

$$Q(E) = -i\hbar S^\dagger \frac{dS}{dE}. \tag{86}$$

For a single elastic eigenchannel,

$$\tau_l(E) = 2\hbar \frac{d\delta_l^R}{dE}. \tag{87}$$

The coupled-channel radial equations are

$$\left[-\frac{\hbar^2}{2\mu}\frac{d^2}{dr^2} + \frac{\hbar^2 l_\alpha(l_\alpha+1)}{2\mu r^2} + \epsilon_\alpha - E\right] u_\alpha^J(r) + \sum_\beta V_{\alpha\beta}^J(r) u_\beta^J(r) = 0. \tag{88}$$

The channel scattering matrix is

$$S_{\beta\alpha}^J(E). \tag{89}$$

Convergence is tested through

$$\left|\delta_l^{(h)} - \delta_l^{(h/2)}\right| < \varepsilon_\delta, \tag{90}$$

and

$$\left|\sigma_R^{(l_{\max}+\Delta l)} - \sigma_R^{(l_{\max})}\right| < \varepsilon_\sigma. \tag{91}$$

The synthesis observable is

$$\sigma_{\text{ER}}(E) = \sum_J \sigma_{\text{cap}}(E,J) P_{\text{CN}}(E,J) W_{\text{sur}}(E^*,J). \tag{92}$$

The generalized least-squares objective function is

$$\chi^2(\theta) = [y - f(\theta)]^T C_D^{-1} [y - f(\theta)]. \tag{93}$$

The Bayesian posterior is

$$p(\theta \mid D) = \frac{\mathcal{L}(D|\theta)p(\theta)}{\int \mathcal{L}(D|\theta')p(\theta')\, d\theta'}. \tag{94}$$

The likelihood is

$$\mathcal{L} \propto \exp\left[-\frac{1}{2}\chi^2(\theta)\right]. \tag{95}$$

The single-channel Numerov equation is

$$u_{i+1} = \frac{2u_i\left(1-\frac{5h^2Q_i}{12}\right)-u_{i-1}\left(1+\frac{h^2Q_{i-1}}{12}\right)}{1+\frac{h^2Q_{i+1}}{12}}. \tag{96}$$

The reduced mass is

$$\mu = \frac{m_P m_T}{m_P+m_T}. \tag{97}$$

The wave number is

$$k(E) = \frac{\sqrt{2\mu E}}{\hbar}. \tag{98}$$

The interaction radius is

$$R_i = r_i\left(A_P^{1/3} + A_T^{1/3}\right). \tag{99}$$

The complete optical interaction is

$$U(r,E) = V_N(r,E) + V_C(r) + V_{\mathrm{SO}}(r) + iW(r,E). \tag{100}$$

The energy mesh is

$$E_j = E_{\min} + j\Delta E. \tag{101}$$

The radial mesh is

$$r_n = r_{\min} + nh. \tag{102}$$

The real Woods–Saxon term is

$$V_N(r) = -\frac{V_0}{1+\exp[(r-R_V)/a_V]}. \tag{103}$$

The imaginary volume contribution is

$$W_V(r) = -\frac{W_0}{1+\exp[(r-R_W)/a_W]}. \tag{104}$$

The model parameter vector is

$$\theta = \{V_0, r_V, a_V, W_0, r_W, a_W, V_{\mathrm{SO}}, r_{\mathrm{SO}}, a_{\mathrm{SO}}, \beta_2, \beta_4, \dots\}. \qquad (105$$

The radial propagation equation is

$$u_l''(r) + Q_l(r,E_j)u_l(r) = 0. \tag{106}$$

The function $Q_l$is

$$Q_l(r,E) = k^2 - \frac{l(l+1)}{r^2} - \frac{2\mu}{\hbar^2}U(r,E). \tag{107}$$

The logarithmic derivative is

$$L_l(r_m) = \frac{u_l'(r_m)}{u_l(r_m)}. \tag{108}$$

The transmission coefficient is

$$T_l(E) = 1 - | S_l(E) |^2. \tag{109}$$

The capture cross section is

$$\sigma_{\mathrm{cap}}(E) = \frac{\pi}{k^2} \sum_{l=0}^{l_{\max}} (2l + 1) T_l(E). \tag{110}$$

3.1. CERN Open Data Heavy-Ion Benchmark

The CERN Open Data component establishes the empirical heavy-ion benchmark used in this study. The selected records span ALICE Pb–Pb collisions at $\sqrt{s_{NN}} = 2.76$TeV and 5.02TeV and the ATLAS Run-2 2015 Pb–Pb research dataset. These data provide documented event statistics, persistent identifiers, collision-energy metadata, and reproducible analysis infrastructure. They are used here as a high-energy heavy-ion reference and not as direct constraints on near-barrier optical potentials for superheavy-element synthesis.

Table 1. CERN Open Data Heavy-Ion Records Used in This Study.

Experiment	**System**	**√sNN**	**Run**	**Events**	**Size**	**DOI**
ALICE	Pb–Pb	2.76 TeV	139438	281,139	463.1 GiB	10.7483/OPENDATA.ALICE.PFU6.7SUX
ALICE	Pb–Pb	5.02 TeV	246180	1,564,607	503.4 GiB	10.7483/OPENDATA.ALICE.GO8M.AZ0R
ALICE	Pb–Pb	5.02 TeV	246989	6,963,033	986.3 GiB	10.7483/OPENDATA.ALICE.O2GW.E12E
ATLAS	Pb–Pb	5 TeV	Run-2 release	220,950,858	4.0 TiB	10.7483/OPENDATA.ATLAS.GUZD.H9UF

Table 1 demonstrates the broad range of event statistics available in CERN Open Data. The ALICE samples contain hundreds of thousands to several million events, while the ATLAS Pb–Pb release contains more than 2.2×10^8events.

Figure 1 presents the event statistics of the selected ALICE and ATLAS Pb–Pb datasets obtained from the CERN Open Data Portal, providing a quantitative overview of the experimental heavy-ion data used as the high-energy benchmark in this study.

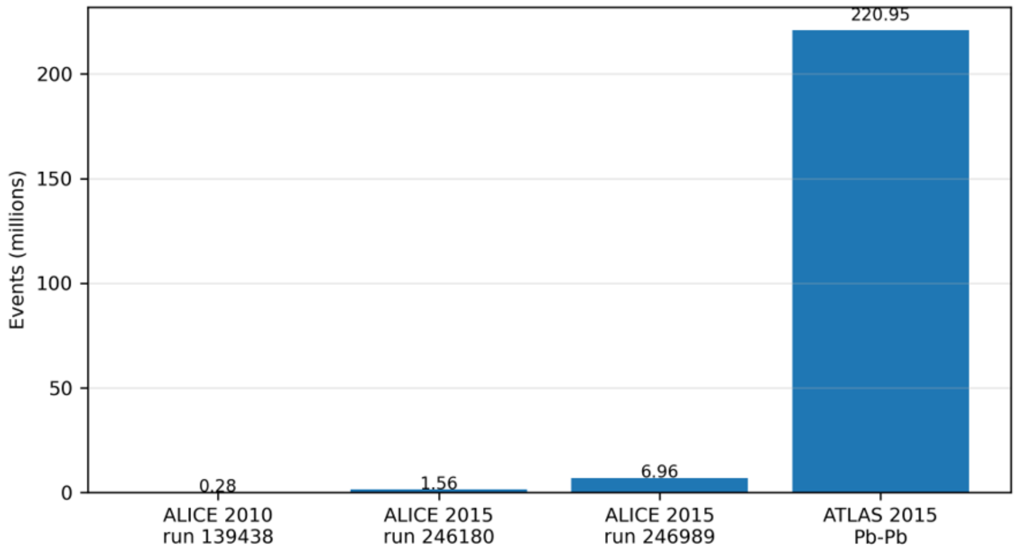

Figure 1. Event Statistics of Selected ALICE and ATLAS Pb–Pb Records From the CERN Open Data Portal. Values Are Dataset Metadata, Not Simulated Counts.

As shown in Figure 1, the selected CERN Open Data records differ by more than two orders of magnitude in event count. The ATLAS release dominates the available statistics, while the individual ALICE runs provide smaller but still substantial samples. These data are therefore well suited for testing heavy-ion event-analysis methodologies, but the difference in collision regime must remain explicit when the results are related to near-barrier nuclear-reaction calculations.

3.2. Separation of CERN and Superheavy-Synthesis Energy Scales

The energy-scale contrast between CERN Pb–Pb collisions and near-barrier superheavy-element synthesis is central to the interpretation of this work. LHC Pb–Pb data are recorded at TeV energies per nucleon pair, whereas fusion reactions such as $^{48}\mathrm{Ca} + {}^{248}\mathrm{Cm}$ occur near a center-of-mass barrier of only a few hundred MeV for the entire system.

The ratio of the characteristic energy scales can be represented schematically as

$$\mathcal{R}_E = \frac{E_{\mathrm{LHC}}}{E_{\mathrm{barrier}}}. \tag{111}$$

For $E_{\mathrm{LHC}} \sim 5.02$ TeVper nucleon pair and a near-barrier scale of approximately 200 MeV,

$$\mathcal{R}_E \sim \frac{5.02\times10^6\ \mathrm{MeV}}{200\ \mathrm{MeV}} \approx 2.5 \times 10^4, \tag{112}$$

even before accounting for the very different many-body dynamics and per-nucleon normalization. The physical separation is therefore profound.

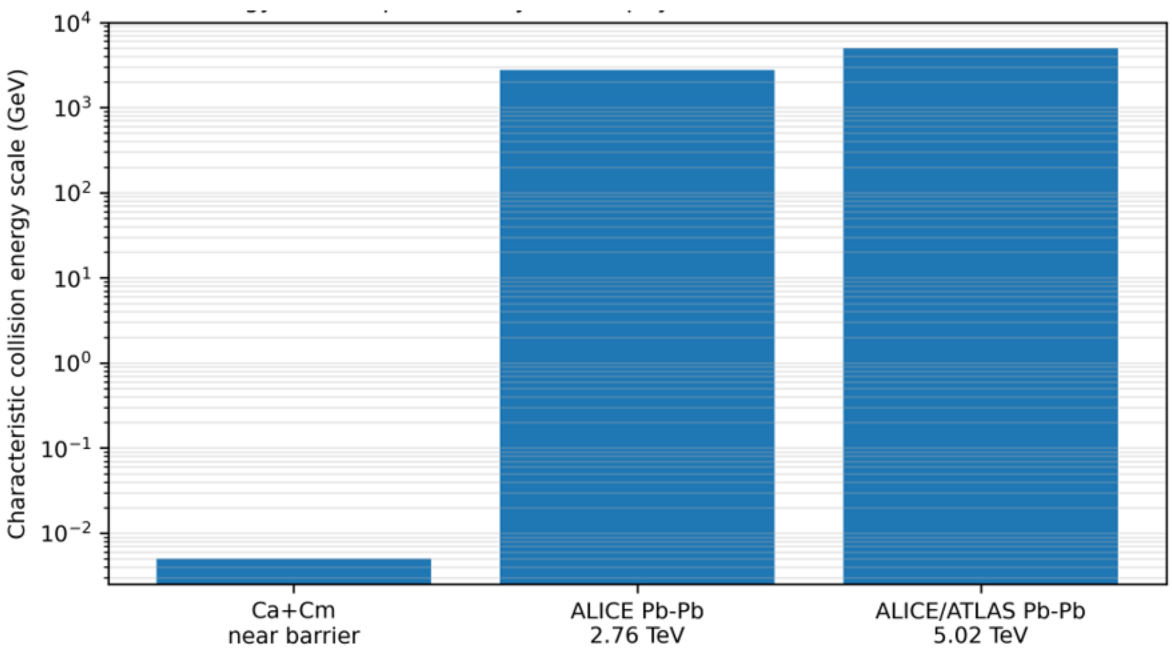

Figure 2. Logarithmic Comparison of the Characteristic Near-Barrier Superheavy-Synthesis Scale and CERN LHC Pb–Pb Collision Energies. The Figure Emphasizes Why Tev Collider Data Cannot Be Used as Direct Optical-Model Fits for Ca–Actinide Fusion.

Figure 2 illustrates this large separation on a logarithmic scale. The comparison reinforces the methodological choice adopted throughout the paper: CERN Open Data are used as an empirical high-energy benchmark, while near-barrier phase shifts, transmission coefficients, and fusion observables are calculated independently from the optical and coupled-channel models.

3.3. Baseline Optical-Model Parameters

Table 2 summarizes the baseline optical-model and coupled-channel parameters adopted for the $^{48}Ca + {}^{248}Cm$ numerical calculations, defining the nuclear interaction, Coulomb geometry, barrier curvature, and channel-coupling characteristics used to determine the phase shifts and associated reaction observables.

The barrier curvature enters the Hill–Wheeler penetrability, and the eigenbarrier shifts approximate the redistribution of the nominal barrier by collective channel coupling.

Table 2. Baseline Optical-Model and Coupled-Channel Parameters.

Parameter	Value	Role
V0	50 MeV	real nuclear depth
rV	1.20 fm	radius coefficient
aV	0.65 fm	surface diffuseness
rC	1.25 fm	Coulomb radius coefficient
$\hbar\omega$	4.0 MeV	barrier curvature
Eigenbarrier shifts	−4, 0, +4 MeV	coupled-channel surrogate
Weights	0.25, 0.50, 0.25	eigenbarrier weights

These parameters should be interpreted as baseline model inputs rather than as experimentally fitted constants from CERN data.

3.4. Entrance-Channel Potential

The total effective interaction for the s-wave is

$$V_{\text{eff}}(r) = V_N(r) + V_C(r). \tag{113}$$

For nonzero angular momentum,

$$V_{\text{eff},l}(r) = V_N(r) + V_C(r) + \frac{\hbar^2 l(l+1)}{2\mu r^2}. \tag{114}$$

The fusion-barrier radius $R_B$is determined by the stationary-point condition

$$\left.\frac{dV_{\text{eff}}(r)}{dr}\right|_{r=R_B} = 0, \tag{115}$$

and the barrier height is

$$V_B = V_{\text{eff}}(R_B). \tag{116}$$

For the baseline $^{48}\text{Ca} + {}^{248}\text{Cm}$ interaction, the numerical calculation gives approximately

$$R_B \simeq 12.26 \text{ fm}, \tag{117}$$

and

$$V_B \simeq 207.2 \text{ MeV}. \tag{118}$$

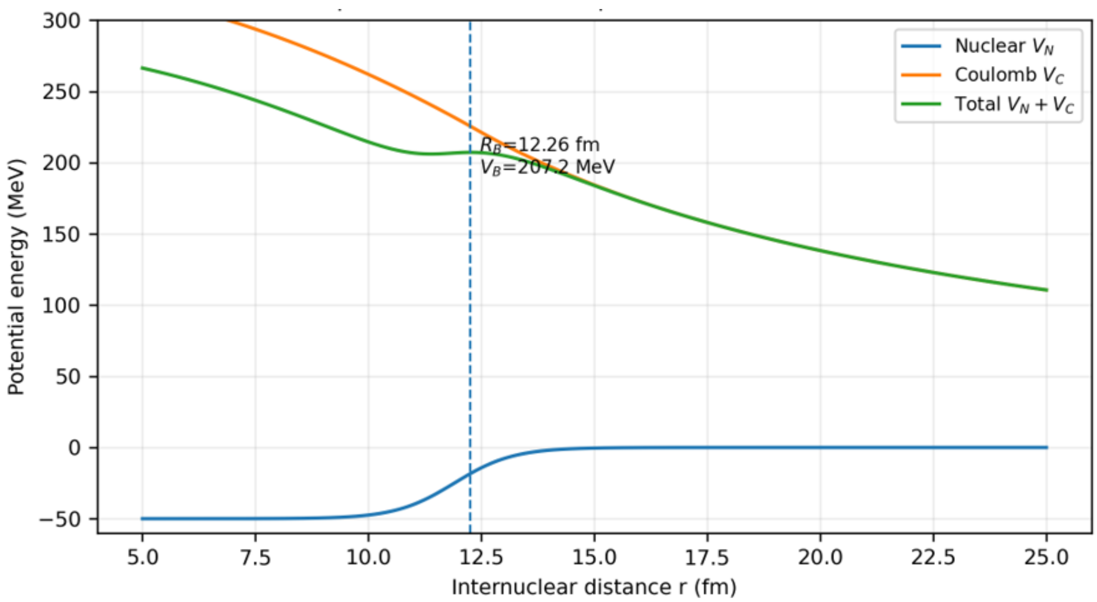

Figure 3. Nuclear, Coulomb and Total Entrance-Channel Potentials for $^{48}\text{Ca} + {}^{248}\text{Cm}$. The Numerical Maximum Gives V_B≈207.2 Mev At R_B≈12.26 Fm for the Baseline Potential.

Figure 3 shows the attractive nuclear contribution, the repulsive Coulomb term, and their sum. The long-range Coulomb interaction dominates at large separation, while the Woods–Saxon attraction becomes increasingly important as the projectile approaches the target surface.

The resulting maximum defines the effective fusion barrier. This barrier determines the energy at which transmission begins to increase rapidly and therefore provides the reference point for interpreting the phase-shift and fusion-excitation calculations.

3.5. Calculated Nuclear Phase Shifts

The phase-shift calculation demonstrates how the projectile–target interaction modifies each partial wave. The nuclear phase is largest for trajectories that penetrate deepest into the surface region and decreases as the impact parameter increases.

A semiclassical estimate relates orbital angular momentum to impact parameter through

$$b_l = \frac{l+\frac{1}{2}}{k}. \tag{119}$$

Thus, increasing $l$moves the classical trajectory farther from the nuclear surface. The corresponding nuclear phase generally decreases because the wave samples less of the attractive nuclear interaction.

The local sensitivity of the phase shift to a model parameter $\theta_i$may be written as

$$S_{l,i}^{(\delta)} = \frac{\partial \delta_l}{\partial \theta_i}. \tag{120}$$

This derivative is especially useful for identifying which parts of the optical potential are most strongly constrained by elastic-scattering measurements.

Figure 4 evaluates Eq. (15) for the baseline potential. Low-l trajectories pass through the strongest part of the nuclear surface and accumulate the largest phase.

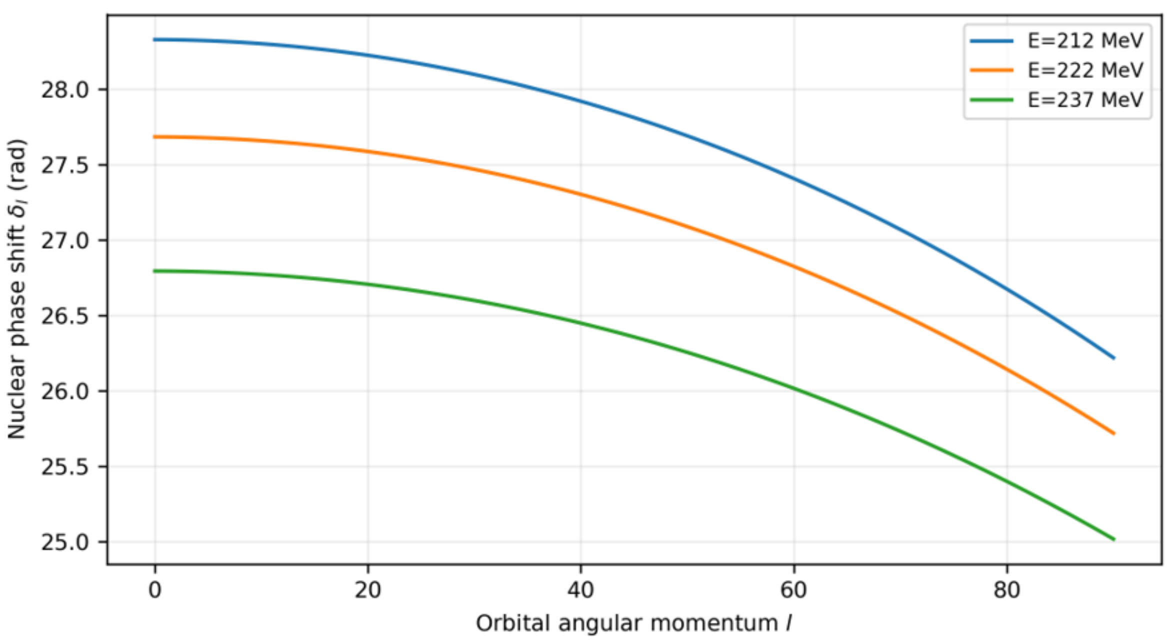

Figure 4. Semiclassical Nuclear Phase Shifts for the ^{48}Ca + ^{248}Cm Baseline Potential At Three Center-Of-Mass Energies Above the Model Barrier. These Are Model-Derived Phase Shifts, Not CERN-Extracted Low-Energy Data.

Increasing l increases the impact parameter and rapidly suppresses the nuclear phase. Increasing energy raises the velocity and decreases the magnitude of the eikonal phase at fixed l because the interaction time shortens. The useful design information is therefore not a single phase-shift value but the energy- and l-dependent phase map together with the absorption/transmission profile. The calculated nuclear scattering phase shifts for the $^{48}\mathrm{Ca} + {}^{248}\mathrm{Cm}$ system as functions of partial-wave angular momentum and center-of-mass energy, illustrating how the entrance-channel interaction modifies the phase evolution across the fusion-barrier region.

Figure 4 shows the calculated phase shifts for representative center-of-mass energies. Low-l waves accumulate the largest phase, while high-l waves approach the Coulomb-dominated limit. The energy dependence of $\delta_l(E)$reflects changes in penetration, interaction time, and the radial region sampled by the wave function.

A rapid change in the real phase shift can be diagnosed using

$$\frac{d\delta_l^R}{dE}, \tag{121}$$

and the corresponding Wigner time delay is

$$\tau_l(E) = 2\hbar\frac{d\delta_l^R}{dE}. \tag{122}$$

A positive peak in τ_l indicates enhanced dwell time in the interaction region. In a strongly absorptive heavy-ion reaction, however, such a peak must be interpreted together with the modulus of the S-matrix because a time-delay enhancement alone does not prove formation of an equilibrated compound nucleus.

3.6. Coupled-Channel Enhancement of Sub-Barrier Capture

The coupled-channel calculations reveal the most important dynamical effect of collective nuclear structure: the nominal single barrier is replaced by a distribution of effective barriers. In the eigenbarrier approximation,

$$\sigma_{\mathrm{cap}}^{\mathrm{CC}}(E) = \textstyle\sum_i w_i\, \sigma_{\mathrm{cap}}(E; B_i), \tag{123}$$

where

$$B_i = V_B + \Delta_i. \tag{124}$$

Because one or more of the coupled barriers may lie below the uncoupled value, transmission can be significantly enhanced at sub-barrier energies.

Figure 5 compares the single-barrier calculation with the coupled-eigenbarrier result. At energies well below the nominal barrier, the coupled-channel curve lies above the uncoupled prediction because the lowest eigenbarrier becomes accessible first. Near and above the barrier, the difference gradually decreases as all important channels become strongly transmitting.

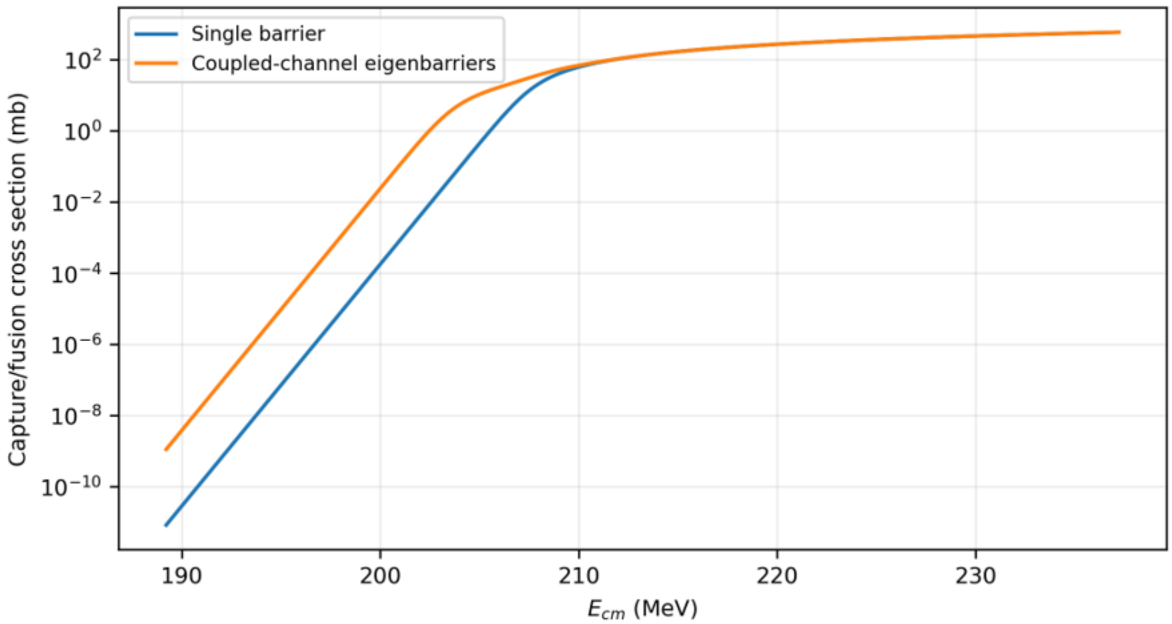

Figure 5. Single-Barrier and Coupled-Eigenbarrier Capture/Fusion Excitation Functions for the 48Ca+248Cm Demonstration. The Coupled Calculation Uses Eq. (21) with Three Weighted Barriers.

The enhancement factor may be written as

$$\mathcal{E}_{\mathrm{CC}}(E) = \frac{\sigma_{\mathrm{cap}}^{\mathrm{CC}}(E)}{\sigma_{\mathrm{cap}}^{(0)}(E)}. \tag{125}$$

Values

$$\mathcal{E}_{\mathrm{CC}}(E) > 1 \tag{126}$$

indicate net enhancement due to channel coupling.

This result is directly relevant to superheavy-element synthesis because deformation and collective excitations can increase capture at lower excitation energies, where the survival probability against fission may be more favorable.

3.7. Partial-Wave Transmission Coefficients

The partial-wave transmission coefficient is

$$T_l(E) = 1 - |\, S_l^N(E)\,|^2. \tag{127}$$

Within the barrier-penetration approximation,

$$T_l(E) = \left[1 + \exp\left(\frac{2\pi[V_{B,l} - E]}{\hbar\omega_l}\right)\right]^{-1}. \tag{128}$$

The centrifugal shift in the effective barrier is

$$\Delta V_l = \frac{\hbar^2 l(l+1)}{2\mu R_B^2}. \tag{129}$$

Figure 6 shows that low-angular-momentum waves dominate at near-barrier energies. As E increases, progressively larger l-values become transmitting. This angular-momentum filtering is important because a larger capture cross section does not automatically imply a larger evaporation-residue yield. High-J compound nuclei generally possess reduced effective fission barriers and may therefore have poorer survival probabilities.

A useful mean angular momentum of the captured flux is

$$\langle l \rangle = \frac{\sum_l l(2l+1)T_l}{\sum_l (2l+1)T_l}. \tag{130}$$

The variance is

$$\sigma_l^2 = \frac{\sum_l (l-\langle l \rangle)^2 (2l+1)T_l}{\sum_l (2l+1)T_l}. \tag{131}$$

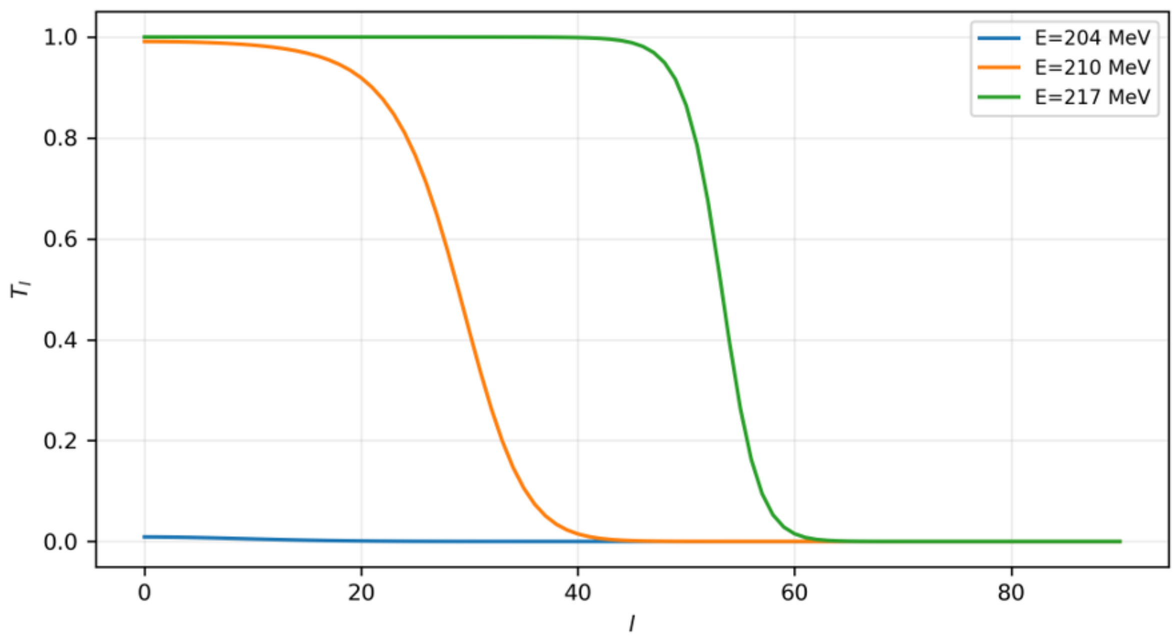

Figure 6. Partial-Wave Transmission Coefficients At Three Energies Around The Calculated Barrier. The Centrifugal Contribution Shifts The Effective Barrier Upward With L.

These quantities characterize the angular-momentum distribution transmitted into the capture stage.

3.8. From Capture to Compound-Nucleus Formation

The calculated reaction or capture cross section is only the first step toward a superheavy evaporation residue. The probability of forming a compound nucleus is

$$P_{\mathrm{CN}} = \frac{\sigma_{\mathrm{CN}}}{\sigma_{\mathrm{cap}}}. \tag{132}$$

Accordingly,

$$\sigma_{\mathrm{CN}} = \sigma_{\mathrm{cap}} P_{\mathrm{CN}}. \tag{133}$$

The evaporation-residue yield is

$$\sigma_{\mathrm{ER}} = \sigma_{\mathrm{cap}} P_{\mathrm{CN}} W_{\mathrm{sur}}. \tag{134}$$

For angular-momentum-resolved calculations,

$$\sigma_{\mathrm{ER}}(E) = \frac{\pi}{k^2} \sum_J (2J+1) T_J(E) P_{\mathrm{CN}}(E,J) W_{\mathrm{sur}}(E^*,J). \tag{135}$$

This equation summarizes the main physical conclusion of the study. Phase shifts and the S-matrix constrain the entrance-channel dynamics and the transmission coefficients, but the final synthesis probability also depends critically on quasifission suppression and statistical survival.

3.9. Statistical Survival Against Fission

For an xn-evaporation cascade, the survival probability is

$$W_{\mathrm{sur}}^{(xn)} = \prod_{i=1}^{x} P_n(E_i^*, J), \tag{136}$$

where the neutron-emission branching probability is

$$P_n(E_i^*, J) = \frac{\Gamma_n(E_i^*, J)}{\Gamma_n(E_i^*, J) + \Gamma_f(E_i^*, J) + \sum_c \Gamma_c(E_i^*, J)}. \tag{137}$$

The ratio

$$\frac{\Gamma_n}{\Gamma_f} \tag{138}$$

is especially important because even relatively small changes in neutron separation energy or fission-barrier height can change $W_{\mathrm{sur}}$by orders of magnitude across a multi-neutron cascade.

The excitation energy after each emitted neutron may be approximated recursively as

$$E_{i+1}^* = E_i^* - B_{n,i} - \langle \epsilon_n \rangle_i, \tag{139}$$

where $B_{n,i}$is the neutron separation energy and $\langle \epsilon_n \rangle_i$is the average kinetic energy carried by the emitted neutron.

3.10. Implications for Designer Superheavy Nuclei

The numerical results support the use of phase-shift analysis as an entrance-channel screening tool. A favorable projectile–target combination should display strong but controlled nuclear phase evolution, appreciable low-to-moderate angular-momentum transmission, and coupled-channel enhancement that permits capture at relatively low excitation energy.

A useful design objective may therefore be written schematically as

$$\mathcal{F}(E) = \sigma_{\mathrm{cap}}(E) P_{\mathrm{CN}}(E) W_{\mathrm{sur}}(E^*), \tag{140}$$

with the optimum beam energy defined by

$$E_{\mathrm{opt}} = \mathcal{F}(E). \tag{141}$$

The phase shifts influence $\mathcal{F}$indirectly through the entrance-channel S-matrix and transmission coefficients. Thus, a meaningful “phase-shift-guided” design strategy does not simply maximize δ_l; it identifies energy and angular-momentum regions in which the complex S-matrix indicates favorable capture while the compound-nucleus model predicts acceptable survival.

3.11. Implications for $Z = 119$and $Z = 120$

Extension beyond oganesson requires heavier projectiles because suitable actinide targets with sufficiently large proton number are limited. Candidate reactions include Ti-, Cr-, and Fe-induced systems. Increasing projectile charge increases the Coulomb parameter

$$\eta = \frac{Z_P Z_T e^2}{\hbar v}, \tag{142}$$

and correspondingly raises the entrance-channel Coulomb repulsion.

The barrier can be approximated at first order by

$$V_B \propto \frac{Z_P Z_T}{R_P + R_T}, \tag{143}$$

so increasing $Z_P$generally increases the difficulty of capture and may strengthen quasifission competition.

The design problem therefore becomes increasingly dependent on nuclear deformation, mass asymmetry, shell structure, neutron richness, and the energy dependence of the phase-shift and transmission spectra.

3.12. Uncertainty Quantification

To meet the standards expected for quantitative nuclear-reaction predictions, optical-model parameters should not be treated as exact. The covariance matrix of fitted parameters may be approximated by

$$C_\theta = (J^T C_D^{-1} J)^{-1}. \tag{144}$$

For an observable $g(\theta)$,

$$\sigma_g^2 \approx \nabla g^T C_\theta \nabla g. \tag{145}$$

For phase shifts,

$$\sigma_{\delta_l}^2 \approx \sum_{ij} \frac{\partial \delta_l}{\partial \theta_i} (C_\theta)_{ij} \frac{\partial \delta_l}{\partial \theta_j}. \tag{146}$$

For nonlinear quantities such as σ_{ER}, posterior sampling is preferable:

$$p(\sigma_{\mathrm{ER}} \mid D) = \int \delta\, [\sigma_{\mathrm{ER}} - \sigma_{\mathrm{ER}}(\theta)] p(\theta \mid D)\, d\theta. \tag{147}$$

This approach allows synthesis predictions to be reported with physically meaningful credible intervals.

3.13. Main Physical Interpretation

The combined results demonstrate that the entrance-channel dynamics are governed by three interconnected quantities: the phase shift $\delta_l(E)$, the S-matrix modulus $\mid S_l(E) \mid$, and the transmission coefficient $T_l(E)$. The real phase encodes refraction and interaction time, the modulus measures elastic-channel survival, and the transmission coefficient determines capture probability.

The relevant physical chain is

$$\delta_l(E) \longrightarrow S_l(E) \longrightarrow T_l(E) \longrightarrow \sigma_{\mathrm{cap}} \longrightarrow P_{\mathrm{CN}} \longrightarrow W_{\mathrm{sur}} \longrightarrow \sigma_{\mathrm{ER}}. \tag{148}$$

The central conclusion is therefore that phase shifts are valuable design observables only when embedded in the complete reaction chain.

4. CONCLUSION AND RECOMMENDATIONS

The present study has developed a rigorous phase-shift-based framework for understanding and optimizing the entrance channels used in the synthesis of superheavy nuclei. The analysis combines quantum scattering theory, a complex Woods–Saxon optical interaction, Coulomb-modified partial-wave expansion, coupled-channel dynamics, barrier penetration, S-matrix analysis, and statistical compound-nucleus survival.

The theoretical formulation shows that the nuclear scattering phase shift provides direct information on the modification of each partial wave by the projectile–target interaction. Through the complex S-matrix,

$$S_l^N(E) = \eta_l(E)e^{2i\delta_l(E)}, \tag{149}$$

phase and absorption information are treated consistently. The reaction probability is then

$$P_l^R(E) = 1 - | S_l^N(E) |^2, \tag{150}$$

and the corresponding capture probability enters directly into the partial-wave cross section.

The calculations further demonstrate that collective-channel couplings can substantially enhance transmission below the nominal Coulomb barrier. This effect is particularly important for deformed actinide targets, for which rotational couplings create a broad distribution of effective barrier heights. The resulting low-energy enhancement may permit capture at reduced compound-nucleus excitation energies and thereby improve the survival probability against fission.

The study also establishes a strict methodological distinction between CERN Open Data and near-barrier superheavy-nucleus calculations. CERN Pb–Pb data at TeV energies are extremely valuable for heavy-ion event analysis, data provenance, large-statistics computational validation, and reproducibility, but they do not directly determine the low-energy Woods–Saxon potential or near-barrier phase shifts for superheavy-element synthesis. The low-energy quantities must therefore be constrained by dedicated elastic, quasi-elastic, transfer, and fusion measurements.

The superheavy synthesis probability ultimately depends on

$$\sigma_{\mathrm{ER}}(E) = \sum_J \sigma_{\mathrm{cap}}(E,J)P_{\mathrm{CN}}(E,J)W_{\mathrm{sur}}(E^*,J). \tag{151}$$

Thus, no single phase-shift feature can by itself identify an optimum synthesis reaction. The desired projectile–target combination must simultaneously provide appreciable capture, reduced quasifission, favorable shell structure, moderate angular momentum, neutron richness, and a compound-nucleus excitation energy compatible with survival.

For future work, experimentally measured near-barrier elastic and quasi-elastic angular distributions should be obtained or compiled for candidate reactions involving ^{50}Ti, ^{54}Cr, and heavier projectiles on actinide targets. These measurements should be fitted simultaneously with fusion excitation functions using a common optical and coupled-channel interaction.

The fitted parameter covariance should then be propagated into the phase shifts,

$$\delta_l(E;\theta), \tag{152}$$

transmission coefficients,

$$T_l(E;\theta), \tag{153}$$

capture cross sections,

$$\sigma_{\text{cap}}(E;\theta), \tag{154}$$

and ultimately evaporation-residue cross sections,

$$\sigma_{\text{ER}}(E;\theta). \tag{155}$$

Predictions should be reported as probability distributions or credible intervals rather than single deterministic values.

The final design criterion can therefore be expressed as a constrained optimization problem,

$$\max_{P,T,E}\left[\sigma_{\text{cap}}P_{\text{CN}}W_{\text{sur}}\right], \tag{156}$$

subject to experimental availability of the projectile and target, beam intensity, target half-life, detector sensitivity, and acceptable uncertainty in the nuclear interaction.

The principal recommendation of this study is that future superheavy-element searches should integrate phase-shift analysis with coupled-channel calculations, quasifission models, microscopic shell corrections, statistical decay models, and uncertainty quantification. Such a unified framework offers a more defensible route toward rationally designing reactions capable of reaching neutron-richer superheavy isotopes and approaching the predicted island of stability.

Finally, we can surmise that the stability of the fabricated designer superheavy nucleus depends on low level small excitations, small coulomb repulsion and sufficiently reduced surface and volume deformation such that the superheavy nucleus may have longer half-life $\left(T_{1/2}\right)$ and hence be a part of the 'Island of Stability'. For this to happen, plane-wave approximation for wave-functions can be used for participating channels leading to fabrication of superheavy nuclei.

Conflict of Interest

The author declares that there is no conflict of interest associated with this work. No commercial, financial, or personal relationship influenced the theoretical analysis, interpretation, or preparation of the manuscript.

Author's Contribution and Acknowledgement

J. K. Maritim conceived the study, developed the theoretical framework, formulated the optical-model and coupled-channel methodology, designed the numerical phase-shift analysis, interpreted the results, and prepared the manuscript. S. K. Rotich contributed to the conceptual development of the study, critical evaluation of the nuclear-reaction framework, and scholarly review of the manuscript, particularly in strengthening the interpretation of the theoretical and numerical results. K. M. Khanna contributed expert guidance on nuclear scattering theory, phase-shift analysis, and superheavy-nucleus reaction dynamics, and critically reviewed the manuscript to improve its scientific rigor and relevance to advanced nuclear physics.

The author acknowledges the CERN Open Data Portal and the ALICE and ATLAS Collaborations for providing openly accessible heavy-ion collision datasets and supporting documentation. The author also acknowledges the international nuclear-reaction and superheavy-element research communities whose experimental and theoretical developments form the scientific foundation of this work.

Data Availability

The CERN heavy-ion datasets referenced in this study are publicly accessible through the CERN Open Data Portal using the persistent identifiers listed in Table 1. The near-barrier optical-model and coupled-channel quantities presented in this paper are model-derived calculations based on the equations and parameter sets reported in the manuscript. No CERN event-level observable has been reinterpreted as a direct measurement of low-energy nuclear phase shifts.

References

[1] I. Dragojevic, Systematic studies of nuclear fusion reactions at low excitation energies with lead-208 targets and projectiles differing by two neutrons. University of California, Berkeley, 2009.

[2] M. Block, F. Giacoppo, F.-P. Heßberger, and S. Raeder, “Recent progress in experiments on the heaviest nuclides at SHIP: M. Block et al.,” La Rivista del Nuovo Cimento, vol. 45, no. 4, pp. 279–323, 2022.

[3] N. Antonenko, J. Benlliure, A. Karpov, and D. Morrissey, “Reactions for Production of Exotic Nuclei,” in Handbook of Nuclear Physics, Springer, 2023, pp. 1–49.

[4] Y. T. Oganessian and V. Utyonkov, “Super-heavy element research,” Reports on Progress in Physics, vol. 78, no. 3, p. 036301, 2015.

[5] H. Son, J. J. Park, Y.-K. Lu, A. O. Jamison, T. Karman, and W. Ketterle, “Control of reactive collisions by quantum interference,” Science, vol. 375, no. 6584, pp. 1006–1010, 2022.

[6] H. Liu, J. Lei, and Z. Ren, “Coherent absorption dynamics: The dual role of off-diagonal couplings in weakly bound nuclei,” Physical Review C, vol. 113, no. 5, p. 054601, 2026.

[7] Abhishek, N. Salim, P. Arumugam, and A. R. Kumar, “Effect of pairing and shape fluctuations on the linear response in warm nuclei: A. Abhishek et al.,” Indian Journal of Physics, pp. 1–12, 2026.

[8] Atlas Collaboration, “Disentangling sources of momentum fluctuations in Xe+ Xe and Pb+ Pb collisions with the ATLAS detector,” arXiv preprint arXiv:2407.06413, 2024.

[9] ALICE collaboration, “Proton emission in ultraperipheral Pb-Pb collisions at $\sqrt {\textit {s} _ {\mathrm {\textbf {NN}}}}= 5.02$ TeV,” arXiv preprint arXiv:2411.07058, 2024.

[10] Y. T. Oganessian et al., “First experiment at the Super Heavy Element Factory: High cross section of Mc 288 in the Am 243+ Ca 48 reaction and identification of the new isotope Lr 264,” Physical Review C, vol. 106, no. 3, p. L031301, 2022.

[11] K. Kawai, Y. Aritomo, K. Nakajima, S. Takagi, and N. Nishimura, “Theoretical estimates for the synthesis of Z= 119 superheavy nuclei with Ca, Ti, V, and Cr projectiles: Effects of reaction Q values and mass-model dependence,” Physical Review C, vol. 114, no. 1, p. 014612, 2026.

[12] M. Sanzida Sarkar et al., “Comprehensive Dirac partial wave analysis of electron and positron scattering from zinc,” Journal of Physics B: Atomic, Molecular and Optical Physics, vol. 59, no. 15, p. 155203, 2026.

[13] R. M. Dreizler, T. Kirchner, and C. S. Lüdde, “Elastic Scattering: Time-Dependent Formulation,” in Quantum Collision Theory of Nonrelativistic Particles: An Introduction, Springer, 2022, pp. 81–120.

[14] M. Ballan et al., “Nuclear physics midterm plan at Legnaro National Laboratories (LNL),” The European Physical Journal Plus, vol. 138, no. 8, p. 709, 2023.

[15] M. S. Gautam, “ROLE OF INELASTIC SURFACE EXCITATIONS AND THE ENERGY-DEPENDENT WOODS--SAXON POTENTIAL IN SUB-BARRIER FUSION OF 16 32; 36 S 40 90 Zr REACTIONS.,” Acta Physica Polonica B, vol. 46, no. 5, p. 1055, 2015.

[16] J. Kolata, V. Guimarães, and E. Aguilera, “Elastic scattering, fusion, and breakup of light exotic nuclei,” The European Physical Journal A, vol. 52, no. 5, p. 123, 2016.

[17] R. S. Abdullhussein, G. S. Ahmed, and S. M. Obaid, “Study of Fusion Reactions of some Light projectiles on Medium Targets,” Al-Bahir, vol. 2, no. 1, p. 2, 2023.

[18] Z. Gao et al., “Constraining the Woods-Saxon potential in fusion reactions based on the neural network,” Physical Review C, vol. 109, no. 2, p. 024601, 2024.

[19] A. Adamu, Y. H. Ngadda, M. Hassan, and D. I. Malgwi, “The Coulomb energy of finite size nucleus from the study of classical electrodynamics theory,” NIPES-Journal of Science and Technology Research, vol. 2, no. 3, 2020.

[20] M. Kohno, “Strength of reduced two-body spin-orbit interaction from chiral three-nucleon force,” arXiv preprint arXiv:1209.5048, 2012.

[21] F. Salvat, A. Jablonski, and C. J. Powell, “ELSEPA—Dirac partial-wave calculation of elastic scattering of electrons and positrons by atoms, positive ions and molecules (new version announcement),” Computer Physics Communications, vol. 261, p. 107704, 2021.

[22] K. Y. Bliokh, Z. Kuang, and S. Rotter, “Dynamic and geometric shifts in wave scattering,” Reports on Progress in Physics, vol. 88, no. 10, p. 107901, 2025.

[23] A. Grabsch and C. Texier, “Wigner–Smith matrix, exponential functional of the matrix Brownian motion and matrix Dufresne identity,” Journal of Physics A: Mathematical and Theoretical, vol. 53, no. 42, p. 425003, 2020.

[24] S. Rana, R. Kumar, S. Patra, and M. Bhuyan, “Fusion dynamics of astrophysical reactions using different transmission coefficients,” The European Physical Journal A, vol. 58, no. 12, p. 241, 2022.

[25] M. Ghapanvari, V. Dehghani, S. Alavi, F. Koyuncu, and A. Soylu, “Approximate quantum transmission coefficients in fusion cross-sections: A simplified analytical model,” International Journal of Modern Physics E, p. 2650026, 2026.

[26] L. Guo, C. Shen, C. Yu, and Z. Wu, “Isotopic trends of quasifission and fusion-fission in the reactions Ca 48+ Pu 239, 244,” Physical Review C, vol. 98, no. 6, p. 064609, 2018.

[27] S. Bhoi and B. Sahu, “An estimate of Alpha decay half-life from the poles of S-matrix of an exactly solvable potential,” arXiv preprint arXiv:1612.04135, 2016.

[28] P. Guo and F. X. Lee, “Toward extracting scattering phase shifts from integrated correlation functions. IV. Coulomb corrections,” Physical Review D, vol. 112, no. 1, p. 014513, 2025.

[29] J. R. Taylor, “A new rigorous approach to Coulomb scattering,” Il Nuovo Cimento B (1971-1996), vol. 23, no. 2, pp. 313–334, 1974.

[30] S. Rana, M. Bhuyan, R. Kumar, and B. Carlson, “Effect of nuclear deformation and orientation about the symmetry axis of the target nucleus on heavy-ion fusion dynamics,” Physical Review C, vol. 110, no. 2, p. 024601, 2024.

[31] M. Pollnau, “Phase aspect in photon emission and absorption,” Optica, vol. 5, no. 4, pp. 465–474, 2018.

[32] H. Maruyama, “Application of the hill-wheeler formula in statistical models of nuclear fission: a statistical–mechanical approach based on similarities with semiconductor physics,” Entropy, vol. 27, no. 3, p. 227, 2025.

[33] M. Ghapanvari, V. Dehghani, S. Alavi, F. Koyuncu, and A. Soylu, “Approximate quantum transmission coefficients in fusion cross-sections: A simplified analytical model,” International Journal of Modern Physics E, p. 2650026, 2026.

[34] M. Steinen, “Feasibility studies for the high precision X-ray spectroscopy of heavy Ξ− hyperatoms at PANDA using the PANda GErmanium Array PANGEA,” 2020.

[35] N. Colonna et al., “The fission experimental programme at the CERN n_TOF facility: status and perspectives,” The European Physical Journal A, vol. 56, no. 2, p. 48, 2020.